JACS
JOURNAL OF THE AMERICAN CHEMICAL SOCIETY
pubs.acs.org/JACS

Article

One Stone, Two Birds: Using High Electric Fields to Enhance the Mobility and the Concentration of Point Defects in Ion-Conducting Solids

Dennis Kemp* and Roger A. De Souza*

Cite This: J. Am. Chem. Soc. 2024, 146, 4783−4794

Read Online

ACCESS | Metrics & More | Article Recommendations

ABSTRACT: Improving the ionic conductivity of outstanding, composition-optimized crystalline electrolytes is a major challenge. Achieving increases of orders of magnitude requires, conceivably, highly nonlinear effects. One known possibility is the use of high electric fields to increase point-defect mobility. In this study, we investigate quantitatively a second possibility that high electric fields can increase substantially point-defect concentrations. As a model system, we take a pyrochlore oxide ($La_2Zr_2O_7$) for its combination of structural vacancies and dominant anti-Frenkel disorder; we perform molecular-dynamics simulations with many-body potentials as a function of temperature and applied electric field. Results within the linear regime yield the activation enthalpies and entropies of oxygen-vacancy and oxygen-interstitial migration, and from three independent methods, the enthalpy and entropy of anti-Frenkel disorder. Transport data for the nonlinear regime are consistent with field-enhanced defect concentrations and defect mobilities. A route for separating the two effects is shown, and an analytical expression for the quantitative prediction of the field-dependent anti-Frenkel equilibrium constant is derived. In summary, we demonstrate that the one stone of a nonlinear driving force can be used to hit two birds of defect behavior.

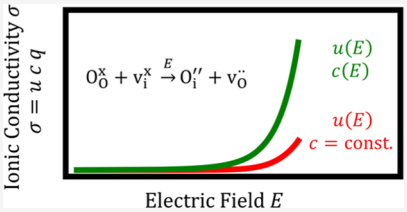

1. INTRODUCTION

Despite the fairly regular discoveries of new crystalline oxides that exhibit outstanding oxide-ion conductivity and the compositional optimization of these new systems, the conductivities of the new, compositional-optimized systems are not vastly superior to those of the already-known oxide-ion conductors.[1−9] Evidently, at least as far as crystal chemistry and crystal composition are concerned, there is a limit to the rate of oxide-ion transport in such materials.[10] Other possibilities for improving the conductivity, such as the introduction of faster diffusion paths[11−14] or the application of mechanical strain,[15−21] have caught, therefore, the community's attention in recent years, but with only moderate success even in the most favorable cases. One promising possibility that has received little attention so far is the use of high electric fields.

The ionic conductivity σ of a material can be expressed as the product of the concentration of the mobile defects c_j, their charge $z_j e$, and their mobility u_j

$$\sigma = \sum_j \sigma_j = c_j |z_j| e u_j \tag{1}$$

Under high electric fields, an (almost) exponential increase of u_j (and thus σ_j) is expected,[22−24] an effect due to the lowering of the migration barrier in the field direction with increasing field strength. This is the first "bird" to be hit with the "stone" of a high electric field, and it is a recognized effect.[4,25−32] A second possibility for increasing the ionic conductivity of a material by applying an electric field—according to eq 1—is to increase the concentration of point defects, c_j. This is the second "bird" to be addressed with the "stone", and it has been considered far less (see Section 1.1).

In order for the "stone" to hit successfully "birds" one and two, the material's structure should provide a network within which point defects (vacancies or interstitials) are mobile; and it should allow such point defects to be generated through the action of an electric field. In the case of oxide-ion transport in a crystalline oxide, the most feasible reaction is the anti-Frenkel (aF) disorder reaction, through which oxygen interstitials and oxygen vacancies are generated (in Kröger−Vink notation[33−35])

$$O_O^x + v_i^x \rightleftharpoons O_i'' + v_O^{\bullet\bullet} \tag{2}$$

Typical crystal structures with highly mobile oxide ions are fluorite oxides (AO_2) and perovskite oxides (ABO_3), but the close-packed nature of such structures gives rise to (prohibitively) high energies for anti-Frenkel disorder.[36−38] One possibility of providing space for oxygen interstitials while

Received: November 15, 2023
Revised: January 15, 2024
Accepted: January 19, 2024
Published: February 12, 2024

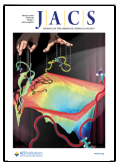

https://doi.org/10.1021/jacs.3c12843
J. Am. Chem. Soc. 2024, 146, 4783−4794

keeping the same basic crystal structure with mobile oxide ions would be to take a material based on an AO_2 fluorite or an ABO_3 perovskite that contains structural vacancies, i.e., sites that are formally vacant in the perfect structure. Structures that fulfill both criteria are thus $A_2B_2O_7$ pyrochlores, based on AO_2 fluorites, and $A_2B_2O_5$ brownmillerites, based on ABO_3 perovskites. The latter system will be considered elsewhere;[39] the former system is the subject of this study.

The $A_2B_2O_7$ pyrochlore structure, part of which is shown in Figure 1, can be described in simplified terms as a highly

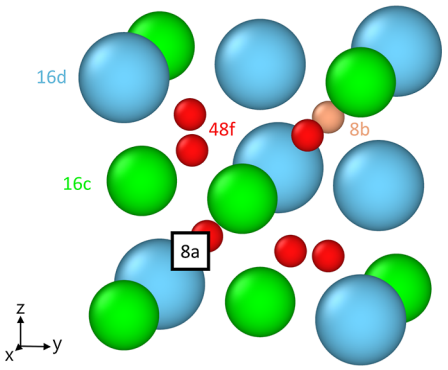

Figure 1. Partial unit cell of the pyrochlore structure with A^{3+} cations in turquoise, B^{4+} cations in green, O^{2-} ions on 48f positions in red, and O^{2-} ions on 8b positions in light red. The structural vacancy at the 8a position is shown as a square.

substituted, oxygen-deficient, ordered fluorite structure. Within this structure, the A^{3+} cations occupy the 16d Wyckoff position, the B^{4+} cations the 16c position, and the O^{2-} ions the 48f and 8b positions. Of major importance for anti-Frenkel disorder is the 8a position, the site of the structural oxygen vacancies. Regular oxide ions can be thermally excited to occupy the 8a site, becoming oxygen interstitial ions and creating thereby oxygen vacancies. All theoretical studies agree that the anti-Frenkel disorder reaction [eq 2] is the most favorable defect formation in $A_2B_2O_7$ pyrochlores and that oxygen diffusion takes place predominantly by a vacancy mechanism between 48f positions.[40−43] It has also been reported[44] that the interstitial ions are mobile, even though the structural vacancies are not adjacent to each other; details of the underlying mechanism, however, have not been elucidated. In any case, we expect both point defects to contribute to the total oxide-ion conductivity, giving rise to two possible contributions to field-enhanced conductivity. In the work performed to date, simulation and experimental studies agree that significant oxygen diffusion only occurs when the cations become disordered or the systems are doped appropriately.[45−49] The main question here is to what extent an electric field can influence the defect formation equilibrium in eq 2 and thus the concentration of charge carriers c_v and c_i without doping or cation disorder.

In this study, $La_2Zr_2O_7$ (LZO) is used as a model pyrochlore oxide for two reasons. First, a many-body interatomic potential set suitable for molecular dynamics (MD) simulations is available.[50,51] In preliminary simulations employing Buckingham pair potentials,[52] only a few point defects were observed (during a reasonably long simulation run) and then only close to the melting temperature. In contrast, in simulations with the many-body potentials, point defects were detected far below the melting point, thus providing a wider range of temperatures for study and also better statistics. Second, according to the many-body potentials, LZO stays in an ordered pyrochlore structure up to its melting point, whereas $Gd_2Zr_2O_7$, for which a many-body potential is also available, shows extensive cation disordering at elevated temperatures, both results in agreement with experimental and computational findings.[53−56] Maintaining an ordered cation arrangement in the simulations is important in order to focus on the effects on anion transport caused by the field rather than the effects caused by cation defects.

In this study, three different LZO systems—oxygen-poor, oxygen-rich, and stoichiometric—are investigated by means of MD simulations as a function of temperature T and field strength E. The results yield, first, a detailed description of oxide-ion conduction and anti-Frenkel disorder in LZO at low field strengths and, in this way, provide a solid base for the investigation of anion-defect behavior at high field strengths. Subsequently, we derive a mathematical expression to describe the field-enhanced formation of anti-Frenkel defects. It is noted that the emphasis is not on LZO as such. LZO simply provides a suitable system for obtaining the MD data that we require in order to derive the mathematical expression. It also provides us with a suitable system for demonstrating the use of various methods to obtain the enthalpy and entropy of anti-Frenkel disorder.

1.1. Literature Review of Field-Dependent Defect Formation. There are a few computational studies that have investigated point-defect formation in an electric field, but they provide no clear picture. Density-functional-theory (DFT) calculations have been conducted on HfO_2,[57] SiO_2,[58] TiO_2,[59] alkaline-earth-metal binary oxides[60] and ABO_3 perovskites.[61] The studies that have addressed anti-Frenkel defect formation[57−59] are similar in that they predict the electric field has an effect on the formation energy of charged defect pairs ($O_i''v_O^{\bullet\bullet}$), but systematic investigations are absent. Furthermore, defect concentrations at finite temperatures were not calculated. (Incidentally, four[57,59−61] of the above studies additionally agree that the formation of neutral oxygen vacancies ($v_O^{\times}$) is affected by strong electric fields.)

MD simulations, on the other hand, are in principle capable of directly yielding $c_{def}(E,T)$, since large systems of the order of 10^4 to 10^5 particles can evolve over several nanoseconds at finite temperatures in the presence of an electric field. Xu et al.[62] have performed a field-dependent study on YSZ with grain boundaries and observed small changes in defect concentration with increasing field strength. The field strengths used (10^{-3} MV cm^{-1}) are, however, orders of magnitude lower than would be expected[63] for a field effect [(10^1 to 10^2)MV cm^{-1}]. Since the Wigner−Seitz (WS) cell method was used to determine the number of point defects, these results should be viewed with caution since the method tends to falsely identify point defects in simulation cells with complex structures, e.g., cells containing extended defects, such as surfaces or grain boundaries.[64] In another study by Schie et al.,[65] field-dependent defect formation was investigated for HfO_2, and a simple model was presented to calculate the critical field strength E_{crit}^{aF} required for the formation of an anti-Frenkel (aF) pair by an oxide ion on a regular lattice site moving a distance d_{vi} to overcome the standard Gibbs formation energy of anti-Frenkel disorder $\Delta G_{aF}^{\ominus}$

$$E_{crit}^{aF} = \frac{\Delta G_{aF}^{\ominus}}{|z_j| e d_{vi}} \tag{3}$$

https://doi.org/10.1021/jacs.3c12843
J. Am. Chem. Soc. 2024, 146, 4783−4794

While the MD results were consistent with the predicted values of eq 3 (no defect generation observed at lower fields), confirmation was not obtained because E_{crit}^{aF} was an order of magnitude higher than the field at which the simulation cells became unstable.

Experimental evidence of a field-dependent defect concentration is rare, as the field strengths required for this are extraordinarily high, and, in addition, field effects must be separated from other voltage-induced effects. Evans et al.[66] applied high field strengths (up to 6 MV cm^{-1})[67] to hexagonal Er(Mn,Ti)O_3 single crystals and found an increase in electrical conductivity of several orders of magnitude, attributing the increase to the formation of anti-Frenkel pair defects. The possibility of stoichiometry polarization was not excluded, however, nor was the possibility of sample decomposition. The authors claimed that support for the stability of anti-Frenkel pairs was provided by MD simulations, but the simulations were only carried out for tens of ps, whereas with respect to experiment, stability is presumably required for hours at the very least.

1.2. Theoretical Prediction of $u_O(E)$. It is important to keep in mind the difference between defect mobilities and ion mobilities. Equation 1 was written in terms of defect quantities, but it could equally well be written in terms of ion quantities. Since ion concentrations are orders of magnitude higher than defect concentrations (by definition), and since there is only one measured conductivity, the ion mobility has to be orders of magnitude lower than the defect mobility. Specifically, for an oxide material with two mobile oxygen defects, the mobility of the oxide ions, u_O, can be described as the weighted sum of each defect's individual mobility (here, oxygen vacancy mobility u_v and oxygen interstitial mobility u_i)

$$u_O = \frac{c_i}{c_O} u_i + \frac{c_v}{c_O} u_v \tag{4}$$

The following description of $u_O(E)$ applies individually to vacancy and interstitial contributions.

The theoretical treatment of $u_O(E)$ assumes that the mobility is proportional to the difference in the forward (f) and reverse (r) jump rates. The quantitative treatment yields

$$u_O = \frac{1}{E}\frac{c_{def}}{c_O} d_O \nu_0 \times \left[\exp\left(-\frac{\Delta G_{mig}^{\ddagger,f}}{k_B T}\right) - \exp\left(-\frac{\Delta G_{mig}^{\ddagger,r}}{k_B T}\right)\right] \tag{5}$$

where d_O is the jump distance, c_{def} is the number density of defects (vacancies or interstitials), c_O is the number density of oxide ions, ν_0 is the jump attempt frequency, k_B is Boltzmann's constant, and T is the temperature. The activation free enthalpies for the forward and reverse jumps, $\Delta G_{mig}^{\ddagger,f}$ and $\Delta G_{mig}^{\ddagger,r}$, are obtained by assuming that the free energy landscape is cosinusoidal and that the field is linearly superimposed on the free energy landscape[68]

$$\Delta G_{mig}^{\ddagger,f/r} = \Delta G_{mig}^{\ddagger}\left[\sqrt{1-\gamma^2} \mp \gamma\left(\frac{\pi}{2}\right) + \gamma \arcsin \gamma\right] \tag{6}$$

with $\gamma = (|z_O| e E d_O)/(\pi \Delta G_{mig}^{\ddagger})$. This approach is superior to the traditional approach[22−24] as it is mathematically exact for a given free energy hypersurface. In the limit of small fields, eq 5 becomes (with $\Delta G_{mig}^{\ddagger} = \Delta H_{mig}^{\ddagger} - T\Delta S_{mig}^{\ddagger}$)

$$u_{O,E\to 0} = \frac{c_{def}}{c_O} d_O^2 \frac{|z_O| e}{k_B T} \nu_0 \exp\left(\frac{\Delta S_{mig}^{\ddagger}}{k_B}\right)\exp\left(-\frac{\Delta H_{mig}^{\ddagger}}{k_B T}\right) \tag{7}$$

i.e., the standard expression for the field-independent mobility is recovered.

The rationale behind this approach, indeed, its specific benefit, is that eq 6 predicts $\Delta G_{mig}^{\ddagger,f/r}(E)$ from the zero-field quantity $\Delta G_{mig}^{\ddagger}$ and from the structural quantity d_O. It obviates the need to calculate individually $\Delta G_{mig}^{\ddagger,f}$ and $\Delta G_{mig}^{\ddagger,r}$ (and the respective d_O values) for each E value of interest. For exceptionally high field strengths ($E \sim 10^{1.5}$ MV cm^{-1}), above which the electrons in a solid will be affected,[69,70] discrepancies are to be expected, but such field strengths are not considered in this study. In cases where exact values are required, DFT calculations of $\Delta H_{mig}^{\ddagger,f/r}$ (see refs 57 and 58) and $\Delta S_{mig}^{\ddagger,f/r}$ would need to be performed.

One of the aims of this study is to derive an analogous expression for defect concentrations that would predict quantitatively $c_{def}(E,T)$ from (easily accessible) zero-field quantities.

2. COMPUTATIONAL METHODS

We used MD simulations to investigate field-dependent ion transport because the method is efficient, has a comparatively low computational cost, and allows u_{def} and c_{def} to be obtained directly from the simulations over large ranges of temperature and field strength. In addition, we need to make no assumptions in advance about the exact migration paths taken (and thus the heights of the migration barriers), and this is important because the pyrochlore structure has a variety of different migration barriers (for vacancies and interstitial transport) due to its three crystallographically different oxygen sites (see Figure 1).

MD simulations were performed by means of the LAMMPS code[71] with periodic boundary conditions in all dimensions. The NpT ensemble with constant particle number N, pressure p, and temperature T was employed, and to ensure this, Nosé−Hoover thermostat and barostat with damping parameters of 0.1 and 10 ps, respectively, were used.[72,73] The pressure of 0 bar was used in all simulations. The long-range Coulombic interactions were calculated with a particle−particle particle−mesh solver[74] with an accuracy of 10^{-5}. Newton's equations of motion were integrated by means of the velocity Verlet algorithm with a time step of 1 fs. The electric field in the simulations was included as an additional force $\mathbf{F}_j = z_j e\mathbf{E}$ acting on each particle. In all simulations, the electric field was applied in the x-direction, and the drift velocity of oxide ions ($v_{d,O}$) in this direction was determined. Specifically, $v_{d,O}$ is obtained easily and reliably from MD simulations[75] by evaluating the mean displacement of all oxide ions, $\langle r_O \rangle$, as a function of simulation time t, according to $v_{d,O} = d\langle r_O\rangle(t)/dt$ (the behavior should be linear, as this indicates steady-state conditions with a constant drift velocity). The mobility u_O is subsequently obtained from

$$u_O = \frac{v_{d,O}}{E} \tag{8}$$

Short-range interactions were modeled with the many-body potential derived by Cooper *et al.*,[50] which is based on the embedded atom method[76] and calculates the potential energy U_j of an atom j as

$$U_j = \frac{1}{2}\sum_k \phi_{\alpha\beta}(r_{jk}) - G_\alpha \sqrt{\sum_k \sigma_\beta(r_{jk})} \tag{9}$$

The first term in eq 9 describes simple pair interactions between two atoms j and k separated by a distance r_{jk}. Here, $\phi_{\alpha\beta}(r_{jk})$ is a combination of Morse and Buckingham potentials

$$\phi_{\alpha\beta}(r_{jk}) = \phi_M(r_{jk}) + \phi_B(r_{jk}) \tag{10}$$

https://doi.org/10.1021/jacs.3c12843
J. Am. Chem. Soc. 2024, 146, 4783−4794

$$\phi_M(r_{jk}) = D_{\alpha\beta}\{\exp[-2\gamma_{\alpha\beta}(r_{jk} - r_0)] - 2\exp[-\gamma_{\alpha\beta}(r_{jk} - r_0)]\} \quad (11)$$

$$\phi_B(r_{jk}) = A_{\alpha\beta}\exp\left(\frac{-r_{jk}}{\rho_{\alpha\beta}}\right) - \frac{C_{\alpha\beta}}{r_{jk}^6} \quad (12)$$

The second term in eq 9 calculates the energy required to introduce an atom j with type α into the electron cloud distribution of the surrounding atoms with atom type β. It is comprised of a pairwise interaction $\sigma_\beta(r_{jk}) = n_\beta/r_{jk}^8$ that is passed through a nonlinear embedding function ($G_\alpha\sqrt{\cdot}$). Though usually used for simulations of metals and alloys, it was demonstrated by Cooper *et al.*[50] that this approach is applicable to ionic systems, too. Specifically, they derived a set of parameters for actinide oxides substituted in CeO_2, including the O−O interactions, and, in a subsequent work,[77] pair potential contributions of lanthanide oxides, including the La−O interactions. These are combined with a second parameter set[51] that includes a Zr−O interaction and the same O−O interaction (see Table 1).

Table 1. Potential Parameters for the Many-Body Potential Used in This Study[a]

$\alpha-\beta$	La−O	Zr−O	O−O	Zr−Zr
$D_{\alpha\beta}$/eV		1.2269		
$\gamma_{\alpha\beta}$/Å^{-1}		1.4482		
r_0/Å		1.998		
$A_{\alpha\beta}$/eV	36197.135	1147.471	830.283	18,600
$\rho_{\alpha\beta}$/Å	0.2069536	0.32235	0.3529	0.23066
$C_{\alpha\beta}$/Å^6	0.000	0.000	3.8843	0.000
G_α/Å$^{1.5}$		1.597	0.69	
n_β/Å^5		1188.786	106.856	

[a]Short-range interactions are calculated with eqs 9−12 using values for La−O taken from ref 77, for Zr−O and Zr−Zr from ref 51, and for O−O from ref 50. The charge numbers of the species are z_O = −1.1104, z_{Zr} = +2.2208, and z_{La} = +1.6656. The short-range interaction cutoff was set to 11.0 Å.

Oxygen transport in stoichiometric LZO was examined in a supercell containing 45,056 ions ($La_{8192}Zr_{8192}O_{28672}$) for the temperature range $2000 \le T/K \le 2875$ and for the range of field strengths $1.0 \le E/MV\ cm^{-1} \le 20.0$. The cells were first equilibrated for 50 ps, and then mean displacements were monitored for another 450 ps. For $E \le 3.0$ MV cm^{-1}, the time of the production run was increased to 950 ps to improve the jump statistics. Two independent runs were conducted at each field strength, and the obtained mobilities were averaged. For oxygen-rich and oxygen-poor LZO, 30 oxygen ions were randomly introduced into the structural vacancies or removed from 48f oxygen positions, ensuring a dilute solution and negligible defect−defect interactions. The excess charge was compensated by increasing/decreasing the charge of the Zr cations. In these systems, u_O was determined as an average over three independent runs for $1000 \le T/K \le 2875$ and $E \le 2.0$ MV cm^{-1}. The cells were equilibrated for 50 ps, and production runs lasted 1450 ps for $T < 2000$ K, 950 ps for $2000 \le T/K \le 2500$, and 450 ps for $T > 2500$ K.

Since we used potentials[50,51,77] that were not derived specifically for LZO, we confirm in Table 2 that the predicted room-temperature lattice parameter and the high-temperature thermal expansion coefficient agree very well with experimental[54,78−80] and computational[81] data.

3. RESULTS AND DISCUSSION

Investigating field-dependent defect migration and formation requires, first of all, knowledge of the field-independent parameters that characterize migration ($\Delta H_{mig}^{\ddagger}$ and $\Delta S_{mig}^{\ddagger}$) and formation ($\Delta H_{aF}^{\ominus}$ and $\Delta S_{aF}^{\ominus}$). This is because increases are relative to the field-independent situation. All these parameters

Table 2. Comparison of Room-Temperature Lattice Parameter a and High-Temperature Thermal Expansion Coefficient a_L (for the Temperature Range $300 \le T/K \le 2500$) with Values from Other Computational (Comp.) and Experimental (Expt.) Studies[a]

a/Å	$a_L/10^{-6}$ K^{-1}	expt./comp.	references
10.830	10.53	comp., MBP	rhis study
10.7997	9.0	expt.	78
10.8128	10.3	expt.	54
10.794	7.0	expt.	79
10.812	7.76	expt.	80
10.828	6.96	comp., EPP	81

[a]The value of ref 81 was converted to a room-temperature lattice parameter. (MBP, many-body potentials; EPP, empirical pair potentials).

are obtained directly from MD simulations rather than from static (i.e., 0 K) simulations, so they refer to the same temperature of interest and the same concentration range of the defects.

In the following, we first obtain for both oxygen vacancies and oxygen interstitials $\Delta H_{mig}^{\ddagger}$ and $\Delta S_{mig}^{\ddagger}$ from u_O at low field strengths. Then, we present and use three methods for extracting $\Delta H_{aF}^{\ominus}$ and $\Delta S_{aF}^{\ominus}$ directly from MD simulations. Subsequently, we analyze the high-field behavior; we show that $u_O(E)$ alone cannot describe the data; we derive a mathematical expression for the description of $c_{def}(E)$; and we demonstrate that the MD results can be described by a combination of $u_O(E)$ and $c_{def}(E)$.

3.1. Oxide-Ion Mobilities at Low Field Strengths.

Anticipating later results as a function of field strength, we consider in Figure 2 the field-independent oxide-ion mobilities,

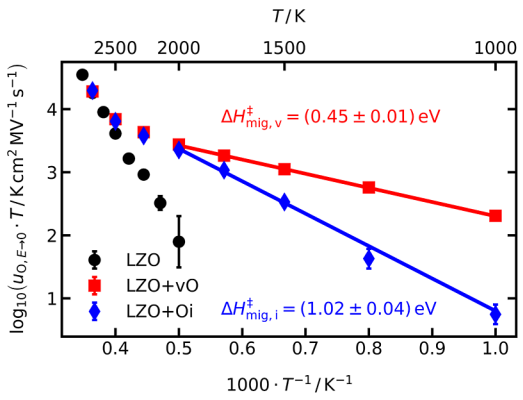

Figure 2. Field-independent oxide-ion mobilities, $u_{O,E\to0}$, as a function of inverse temperature obtained for the three different systems LZO (stoichiometric), LZO+vO, and LZO+Oi. The activation enthalpies of migration, $\Delta H_{mig,v}^{\ddagger}$ and $\Delta H_{mig,i}^{\ddagger}$, are obtained by weighted linear regression of eq 7 to the data.

$u_{O,E\to0}$, obtained for $E \le 2.0$ MV cm^{-1}. Three different systems are considered: $La_2Zr_2O_{7-\delta}$ with extrinsic oxygen vacancies (LZO+vO); $La_2Zr_2O_{7+\delta}$ with extrinsic oxygen interstitials (LZO+Oi); and stoichiometric $La_2Zr_2O_7$ (LZO). As expected, the two nonstoichiometric systems exhibit a low-temperature extrinsic regime governed by the purposely introduced defects and a high-temperature intrinsic regime where both systems behave identically to each other and to the stoichiometric system. The extrinsic regimes (at $T \le 2000$ K) are characterized by negligible contributions from intrinsically generated defects.

https://doi.org/10.1021/jacs.3c12843
J. Am. Chem. Soc. 2024, 146, 4783−4794

Analyzing these regions with eq 7 to extract activation enthalpies and entropies requires the jump length of oxygen vacancies/interstitials, $d_{v/i}$, and the attempt frequency ν_0. For the latter, we use the experimentally determined Debye temperature[82,83] of $\Theta_D \approx 550$ K to obtain $\nu_0 = \Theta_D k_B/h = 11.5$ THz (with h being Planck's constant). The jump length of oxygen vacancies refers to the shortest distance between two 48f positions, $d_v = 2.8$ Å. As mentioned in Section 1, interstitial oxide-ion transport in pyrochlores is not well characterized. Analysis of the trajectories of our simulations shows that interstitial ion transport occurs by means of an extended interstitialcy mechanism involving three oxide ions. Specifically, an interstitial ion on the 8a site jumps toward an occupied, adjacent 48f position, pushing this oxide ion away. This displaced ion pushes, in turn, a third oxide ion from its 48f site onto an adjacent, empty 8a site, forming an interstitial. We also observed a few interstitialcy events involving even more oxide ions, but since the time resolution was only 1 ps, it is unclear if such events were in fact two three-oxide-ion interstitialcy events, one after the other; these jumps are ignored since the majority of jumps involved only three oxide ions. Since for ion transport in a field, the distance traveled by the charge is crucial, we define the jump distance of interstitial transport as the distance between the two nearest 8a positions, $d_i = 7.7$ Å.

Our analysis of the data in Figure 2 with eqs 6 and 7 (and substituting d_O with d_v and d_i, respectively) thus yields $\Delta H^{\ddagger}_{mig,v} = (0.45 \pm 0.01)$ eV and $\Delta S^{\ddagger}_{mig,v} = -(1.24 \pm 0.04)\ k_B$ for oxygen-vacancy migration in LZO+vO; and $\Delta H^{\ddagger}_{mig,i} = (1.02 \pm 0.04)$ eV and $\Delta S^{\ddagger}_{mig,i} = -(0.05 \pm 0.28)\ k_B$ for oxygen-interstitial migration in LZO+Oi. Experimental conductivity studies of $La_{1.95}Sr_{0.05}Zr_2O_{6.975}$ (i.e., a system with oxygen vacancies) report activation energies of (0.4 to 0.6) eV,[84,85] in excellent agreement with our value of $\Delta H^{\ddagger}_{mig,v} = (0.45 \pm 0.01)$ eV.

Extrapolating the data for the extrinsic regimes in Figure 2 to lower and higher temperatures, one recognizes that the vacancies are far more mobile than the interstitials for $T \leq 1000$ K and that the two mobilities are comparable for $T \geq 2000$ K. Consequently, in the intrinsic regime, thermally generated vacancies and interstitials both contribute to the observed mobility. In the next section, these data are used, as one of three methods, to extract $\Delta H^{\ominus}_{aF}$ and $\Delta S^{\ominus}_{aF}$.

3.2. Determination of $\Delta H^{\ominus}_{aF}$ and $\Delta S^{\ominus}_{aF}$ from MD Simulations. The equilibrium constant of anti-Frenkel disorder [eq 2] can be written as

$$K_{aF} = \frac{c_i c_v}{c_{is} c_O} = \exp\left(\frac{\Delta S^{\ominus}_{aF}}{k_B}\right)\exp\left(-\frac{\Delta H^{\ominus}_{aF}}{k_B T}\right) \tag{13}$$

where $\Delta H^{\ominus}_{aF}$ and $\Delta S^{\ominus}_{aF}$ are the enthalpy and entropy of anti-Frenkel defect formation, respectively. The concentrations of oxygen interstitials, oxygen vacancies, interstitial sites ($v_i^{\times}$, i.e. structural vacancies), and oxygen ions ($O_O^{\times}$) are denoted by c_i, c_v, c_{is}, and c_O, respectively. If no other point-defect reactions occur in the simulation cells, charge neutrality requires that $c_v = c_i$. The equilibrium concentration of defects formed by the anti-Frenkel disorder reaction is thus

$$c_v = c_i = \sqrt{c_O c_{is}}\exp\left(\frac{\Delta S^{\ominus}_{aF}}{2k_B}\right)\exp\left(-\frac{\Delta H^{\ominus}_{aF}}{2k_B T}\right) \tag{14}$$

In the following, c_{def} always refers to the concentration of anti-Frenkel defects ($c_{def} \equiv c_v = c_i$).

Since, to the best of our knowledge, the direct determination of $\Delta H^{\ominus}_{aF}$ and $\Delta S^{\ominus}_{aF}$ from MD simulations has not been carried out, we employ three different methods to determine these quantities. Achieving good agreement between the three methods would indicate that the methods are reliable.

3.2.1. Comparison of Extrinsic and Intrinsic Systems. The first method we used for determining $\Delta H^{\ominus}_{aF}$ and $\Delta S^{\ominus}_{aF}$ from MD simulations is based on the experimentalist's approach of comparing the conductivity (or ion mobilities) of systems displaying extrinsic and intrinsic behavior. First, defect mobilities u_i and u_v were calculated from the extrinsic-regime data of the systems LZO+Oi and LZO+vO (Figure 2) with the appropriate forms of eq 4. With this information, the intrinsic-regime data for LZO was analyzed. Specifically, the combination of eqs 4 and 14 gives an expression that was fitted to the u_O data for LZO (see Figure 3), yielding $\Delta H^{\ominus}_{aF} = (5.32 \pm 0.01)$ eV and $\Delta S^{\ominus}_{aF} = (11.48 \pm 0.22)\ k_B$. From the individual contributions, one sees in Figure 3 that, at these high temperatures, the contribution from interstitials is larger than that from vacancies.

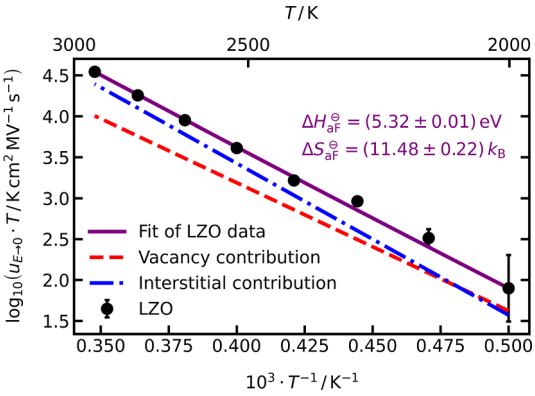

Figure 3. Field-independent oxide-ion mobilities, $u_{O,E\to 0}$, as a function of inverse temperature for stoichiometric LZO. The purple (solid) line is a weighted fit of eqs 4 and 14 to $u_{O,E\to 0}$, and the red (dashed) and blue (dashed-dotted) lines are the individual contributions from vacancy and interstitial mobility, respectively.

3.2.2. WS Analysis. The second method for determining $\Delta H^{\ominus}_{aF}$ and $\Delta S^{\ominus}_{aF}$ from dynamic simulations is unique to the simulator's toolbox, namely counting the point defects present in the LZO simulation cell at each temperature. While simple in principle, reliably determining the number of defects in a dynamic system is difficult in practice since the ions are in motion and not at fixed points in space.

One easily implemented, and thus frequently applied, solution is the WS cell method. A simulation cell is divided into WS cells based on a reference structure (usually the perfect crystal lattice) so that each WS cell contains exactly one lattice site. Snapshots from MD simulations are subsequently mapped onto the WS cells, and the differences are counted as defects, with unoccupied WS cells being identified as vacancies and doubly occupied WS cells as interstitial ions. The major problem is that large-amplitude vibrational motion of ions may lead to such events being counted erroneously as point defects. As a result, we analyze the two nonstoichiometric systems in addition to the stoichiometric system. The difference between the number of counted defects and intentionally inserted defects in the nonstoichiometric systems should equal the number of defects counted in LZO. If the numbers are different, this is a sign of such falsely identified defects.

https://doi.org/10.1021/jacs.3c12843
J. Am. Chem. Soc. 2024, 146, 4783−4794

For the three systems, c_{def} was obtained with the WS analysis, as implemented in the postprocessing software OVITO.[86] Only oxygen vacancies and oxygen interstitials were found (no cation defects), and the results are shown in Figure 4. As expected, we find a steady increase of c_{def} with increasing temperature in LZO, which can be attributed solely to the anti-Frenkel equilibrium. Fitting eq 14 with a weighted linear regression to the data, $\Delta H^{\ominus}_{aF} = (5.21 \pm 0.15)$ eV and $\Delta S^{\ominus}_{aF} = (13.14 \pm 0.33)\ k_B$ are obtained, in good agreement with the values determined with the first method (see Figure 3).

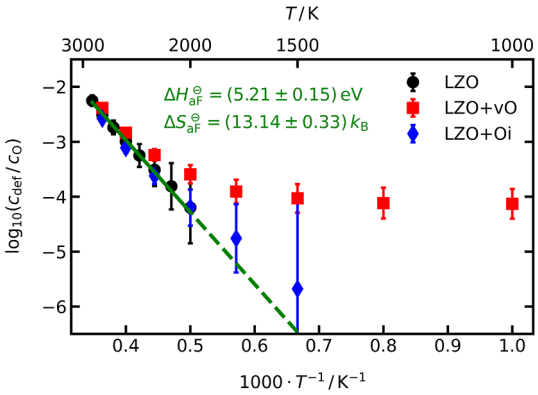

Figure 4. Temperature-dependent relative defect concentration, c_{def}/c_O, obtained with the WS analysis for the three different systems LZO, LZO+vO, and LZO+Oi. Anti-Frenkel formation enthalpy and entropy, $\Delta H^{\ominus}_{aF}$ and $\Delta S^{\ominus}_{aF}$, are obtained by fitting eq 14 with a weighted linear regression to the LZO data. For LZO+Oi, data of the lowest two temperatures are not shown because there were no additional defects detected over the whole simulation time.

Tests of the WS cell method revealed for the vacancy system (LZO+vO) a constant offset of c_{def} at lower temperatures instead of a steady decrease, as observed for LZO. This offset is attributed to large relaxations of oxide ions adjacent to oxygen vacancies. In fact, repeating the simulations with a smaller number of oxygen vacancies led to a reduction of the offset at lower temperatures and thus support the assumption of an artefact. For the interstitial system (LZO+Oi), on the other hand, the WS analysis gave (within error) similar values to the (extrapolated) values of LZO and, in addition, identified no defects below 1500 K. These tests, combined with the similar values of $\Delta H^{\ominus}_{aF}$ and $\Delta S^{\ominus}_{aF}$ compared to the first method, indicate that the application of the WS analysis provides, in the case of LZO, meaningful values, but that the success of the method is not guaranteed, even for a single system.

3.2.3. Excess Heat Capacity. Originally proposed by Mott and Gurney[23] in 1940 and first used experimentally in the 1950s,[87−89] the third method is also copied from the experimental world. It concerns the anomalous increase in a solid's heat capacity on account of defect formation as the melting point is approached. The measured heat capacity thus has two contributions

$$C_p(T) = C_p^0(T) + \Delta C_p(T) \tag{15}$$

$C_p^0(T)$ refers to the heat capacity of the solid without point defects and $\Delta C_p(T)$ to the contribution from point defects ($=\partial \Delta H_{def}/\partial T$). In the case of anti-Frenkel disorder, $\Delta H_{def} = (c_{def}/c_O) N_O \Delta H^{\ominus}_{aF}$ (with N_O being the number of oxygen ions), one obtains

$$\Delta C_p = N_O \sqrt{c_{is}/c_O} \exp\left(\frac{\Delta S^{\ominus}_{aF}}{2k_B}\right) \frac{\Delta H^{\ominus 2}_{aF}}{2k_B T^2} \exp\left(-\frac{\Delta H^{\ominus}_{aF}}{2k_B T}\right) \tag{16}$$

Thus, a plot of $\ln(T^2 \Delta C_p)$ versus $1/T$ yields $\Delta H^{\ominus}_{aF}$ from the slope and $\Delta S^{\ominus}_{aF}$ from the intercept, once $\Delta H^{\ominus}_{aF}$ is known.

To this end, we conducted short (50 ps) MD simulations of LZO for temperatures $300 \le T/K \le 2900$ and determined the average total energy of the system, U_{tot}, at each temperature. We then described $U_{tot}(T)$ over the entire temperature range with cubic splines (not shown); assuming reasonably $H_{tot} \approx U_{tot}$, we obtained $C_p(T) = (\partial H_{tot}/\partial T)_p$ by differentiating the spline function. The results are shown in Figure 5a. To extract $\Delta C_p(T)$ from $C_p(T)$, one requires $C_p^0(T)$ for the temperature range of interest, and this is generally obtained by extrapolating $C_p(T)$ from a range of lower temperatures, for which anti-Frenkel disorder is negligible. We identified the relevant temperature range of $C_p^0(T)$ from Figure 2 (mobility data) and in particular Figure 4 (WS analysis), both of which indicated no anti-Frenkel defects in the simulation cells for $T \le 1500$ K, and we then described these data with a second-order polynomial to obtain $C_p^0(T)$. Extrapolating, now, $C_p^0(T)$ to $T > 1500$ K, we find an increasing difference between the extrapolated C_p^0 and the

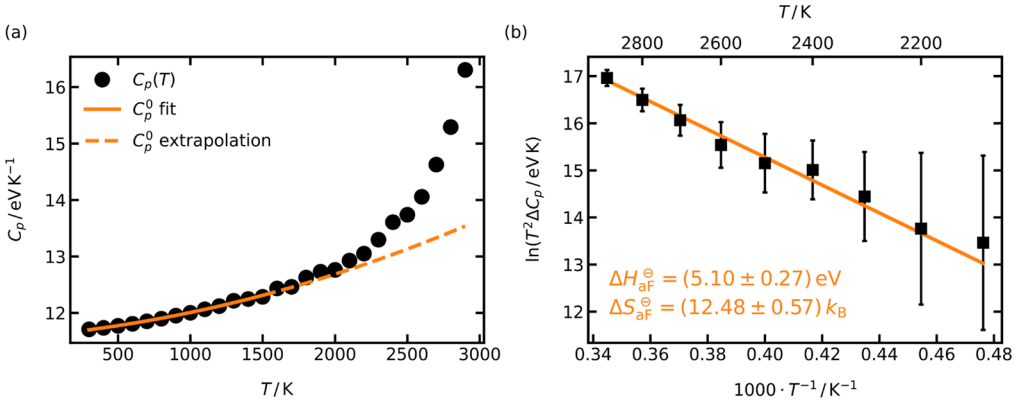

Figure 5. (a) Heat capacity at constant pressure, C_p, obtained from differentiating a cubic spline fit of the temperature-dependent cell energies, $C_p = dU_{tot}/dT$. The solid line represents a second-order polynomial fit up to 1500 K, the temperature range with negligible amounts of anti-Frenkel defects. The dashed line is an extrapolation of the polynomial fit to 2900 K. (b) Excess heat capacity, ΔC_p, calculated as the difference between the defect-free system [extrapolated values, dashed line in (a)] and the observed system (black circles). The values for $\Delta H^{\ominus}_{aF}$ and $\Delta S^{\ominus}_{aF}$ were obtained by fitting eq 16 with a weighted linear regression to the data. Error bars are based on the uncertainties of the second-order polynomial fit [solid line in (a)].

https://doi.org/10.1021/jacs.3c12843
J. Am. Chem. Soc. 2024, 146, 4783−4794

calculated $C_p(T)$ for $T > 2000$ K, i.e., $\Delta C_p(T)$. A fit of eq 16 to the ΔC_p data, as shown in Figure 5b, yields $\Delta H^{\ominus}_{aF} = (5.10 \pm 0.27)$ eV and $\Delta S^{\ominus}_{aF} = (12.48 \pm 0.57)\ k_B$, values in good agreement with those obtained from the previous two methods.

3.2.4. Summary and Comparison. The very good agreement between the values of $\Delta H^{\ominus}_{aF}$ and $\Delta S^{\ominus}_{aF}$ determined by three methods—combination of defect mobilities, WS analysis, excess heat capacity analysis—is a strong result for the determination of defect numbers from dynamic simulations, and the subsequent calculation of $\Delta H^{\ominus}_{aF}$ and $\Delta S^{\ominus}_{aF}$ is not trivial. Consideration of all three data sets together gives $\Delta H^{\ominus}_{aF} \approx (5.2 \pm 0.1)$ eV and $\Delta S^{\ominus}_{aF} \approx (12 \pm 1)\ k_B$.

Since there are no experimental data available for comparison of $\Delta H^{\ominus}_{aF}$ and $\Delta S^{\ominus}_{aF}$, we turn to values obtained from (static) simulations. DFT calculations predict $\Delta H^{\ominus}_{aF}$ of (0.5 to 1.0) and 1.7 eV,[90] with EPP calculations predicting (6.4 to 7.2) and 6.12 eV. The DFT calculations were performed with both vacancy and interstitial in the same small supercell of only 88 atoms, and hence the influence of defect−defect interactions on these values is unclear. The EPP results, in contrast, refer to infinite dilution. Our value of $\Delta H^{\ominus}_{aF}$ is much closer to the EPP values, and it was obtained for a finite, but low, defect concentration range of $10^{-6} \leq c_{def}/c_O < 10^{-2}$ (over a temperature range of $2000 \leq T/K \leqslant 2875$). We consider our value, therefore, to be physically reasonable.

Values of $\Delta S^{\ominus}_{aF}$ are not available for LZO, or indeed, for any pyrochlore material. The two closest cases are CeO_2, for which Grieshammer et al.[91] obtained $\Delta S^{\ominus}_{aF} = 10\ k_B$ from DFT calculations, and In_2O_3, for which Walsh et al.[92] obtained $\Delta S^{\ominus}_{aF} = 5.8\ k_B$ from EPP calculations. Since our value of $\Delta S^{\ominus}_{aF} \approx (12 \pm 1)\ k_B$ is of a similar order of magnitude, we also consider this value to be physically reasonable.

The investigation of the high-field behavior relies on a precise description of the system at low field strengths at the temperatures and defect concentrations examined. With these results, we have such a precise description of the low-field behavior of LZO and can now turn to the influence of high electric fields on defect formation and migration.

3.3. High-Field Behavior of LZO. Oxide-ion mobilities u_O were obtained from MD simulations of LZO at field strengths of $1.0 \leq E/MV\ cm^{-1} \leq 20.0$ and temperatures of $2000 \leq T/K \leq 2875$. For some combinations of very high field strengths and high temperatures, the crystalline structure became amorphous during the MD simulation, as indicated by the loss of long-range order in the radial distribution functions (not shown). Closer examination of such cells before amorphization revealed the presence of cation vacancies on both cation sublattices, as well as cation interstitials and cation antisite defects. Since our primary interest in this study is anti-Frenkel disorder, the presence of other point defects in simulation cells would complicate the analysis, and hence we did not consider u_O data from those simulations in which cation point defects were detected. The mobilities obtained from the remaining simulations are shown in Figure 6.

The qualitative behavior is as expected, that is, constant u_O at low field strengths (here, up to 2.0 MV cm^{-1}) and a nonlinear increase at higher field strengths. The large scatter in u_O for $T <$ 2375 K is a result of poor jump statistics, i.e., only a small number of ion jumps in the field direction took place during the simulation time of 1.5 ns. Returning briefly to those cells that became amorphous during the simulations, we compare the field strength required for amorphization at a given temperature (e.g., $E = 20.0$ MV cm^{-1} at $T = 2375$ K) with E^{mig}_{crit}, the critical field

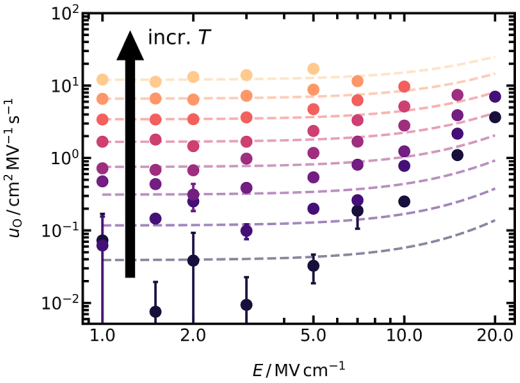

Figure 6. Field-dependent oxide-ion mobilities u_O obtained from MD simulations of LZO in the range of $2000 \leq T/K \leq 2875$ (with 125 K steps). Every data point is the average of two independent runs, with their standard deviation included as error bars. Dashed lines are predictions of u_O with eqs 4−6.

strength at which a crystalline phase becomes unstable because the ions are no longer confined to potential wells, i.e., the migration barrier in one direction goes to zero [specifically, γ in eq 6 goes to zero]. Assuming that $\Delta G^{\ddagger}_{mig,v}$ will be the first barrier to go to zero, we predict with

$$E^{mig}_{crit} = \frac{\pi \Delta G^{\ddagger}_{mig,v}}{|z_i| e d_v} \tag{17}$$

that the critical field strength is much higher, $E^{mig}_{crit} \approx 69$ MV cm^{-1}. This comparison does not take into account, however, the presence of cation point defects in the simulation cells prior to amorphization. In particular, theoretical and experimental studies show that small amounts of cation disorder reduce the activation barrier of oxide-ion migration by (0.3 to 0.5) eV,[41,93] with the consequence that $E^{mig}_{crit} \approx (40$ to $26)$MV cm^{-1}, and thus are in better agreement with the observed behavior in the simulations.

Coming back now to the main topic and Figure 6, we compare the simulation data with the predictions of Section 1.2, taking into account $u_v(E)$ and $u_i(E)$. One perceives that there is a substantial discrepancy for $E > 7$ MV cm^{-1}, which strongly suggests the occurrence of field-enhanced defect formation. Of course, this comparison assumes that the standard treatment of Section 1.2 is applicable to vacancy and interstitial migration in LZO. Since there are no reasons, however, to suspect that the treatment is invalid at these field strengths,[68,75,94] we attribute the discrepancy to the field-enhanced formation of ionic charge carriers.

Unambiguous support for field-enhanced defect formation is provided by a WS analysis (cf. Section 3.2.2) of the same simulation cells from which $u_O(E)$ was obtained (Figure 6). From the analysis, we obtain defect concentrations as a function of E and T, and we plot the results in Figure 7. Also shown (as dashed lines) are the field-independent defect concentrations from Figure 4. Substantial deviations between the symbols and the lines are apparent for $E > 7$ MV cm^{-1}. The degree of deviation increases with increasing field and with decreasing temperature, reaching 2 orders of magnitude for the lowest temperature and highest field examined. For an increase of 1 order of magnitude at, say, $T = 2000$ K, a field of 10 MV cm^{-1} is necessary.

From the data in Figure 7, an effective defect formation enthalpy can be calculated according to

https://doi.org/10.1021/jacs.3c12843
J. Am. Chem. Soc. 2024, 146, 4783−4794

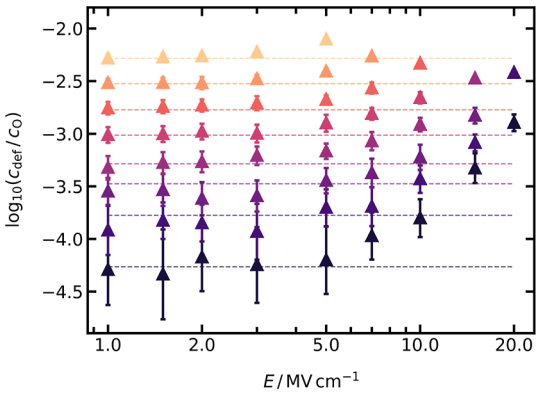

Figure 7. Field-dependent relative defect concentration, c_{def}/c_O, determined with the WS analysis in the range of $2000 \leq T/K \leq 2875$ (with 125 K steps). Every data point is the average of two independent runs, with their standard deviation included as error bars. Dashed lines are the field-independent c_{def}/c_O values determined for LZO from Figure 4.

$$\Delta H^{\ominus}_{aF,eff} = -2k_B \frac{d\ln(c_{def})}{d(1/T)} \tag{18}$$

The results are shown in Figure 8, and they indicate that $\Delta H^{\ominus}_{aF,eff}$ is hardly affected by the electric field up to 7 MV cm^{-1} but

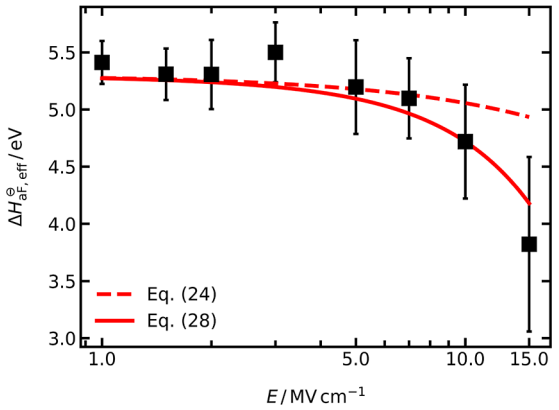

Figure 8. Effective anti-Frenkel defect formation enthalpy, $\Delta H^{\ominus}_{aF,eff}$, calculated with eq 18 from c_{def} in Figure 7. The dashed line is a prediction with eq 24, and the solid line is a fit of eq 28 with $\Delta H^{r} = 9$ meV. For both predictions, $\Delta H^{\ominus}_{aF} = 5.3$ eV was used.

decreases strongly at higher field strengths. This is consistent with the deviation of u_O from the prediction of the standard analytical model observed in Figure 6. At $E > 7$ MV cm^{-1}, the anti-Frenkel disorder reaction is enhanced by the field-induced decrease of $\Delta H^{\ominus}_{aF,eff}$, and consequently, the charge-carrier concentration increases. It is important to note that the field strength of 7 MV cm^{-1} is specific to this system and to the examined temperature range.

3.3.1. An Analytical Expression for $\Delta H^{\ominus}_{aF}(E)$. The formation of $v_O^{\bullet\bullet}$ and O_i'' through anti-Frenkel disorder takes place through a series of steps,[92] such as

$$O_O^{\times} + v_i^{\times} \overset{(i)}{\rightleftharpoons} (v_O O_i)^{\times} \overset{(ii)}{\rightleftharpoons} v_O^{\bullet\bullet}\cdots O_i'' \overset{(iii)}{\rightleftharpoons} v_O^{\bullet\bullet} + O_i'' \tag{19}$$

That is, it starts [step (i)] with an oxide ion on a regular lattice site moving to a vacant interstitial site, forming the defect associate $(v_O O_i)^{\times}$. The vacancy and/or the interstitial move subsequently away from each other [step (ii)], but remain at finite separation. Further movement results eventually in the vacancy and interstitial being separated sufficiently far from one another to count as effectively noninteracting [step (iii)]. The Gibbs energy of anti-Frenkel disorder, $\Delta G^{\ominus}_{aF}$, refers to the difference between the initial and final states, whereas the relevant Gibbs energy for the field-driven process is the difference between the initial and second configuration (or even the initial and third configuration) in eq 19, with $v_O^{\bullet\bullet}$ and O_i'' separated by d_{vi}.

Before deriving a quantitative expression, we return to the simple equation derived by Schie et al.[65] [eq 3] to predict the critical field strength needed for enhanced defect formation. As mentioned in the previous paragraph, the critical issue is the values of d_{vi} and $\Delta G^{\ominus}_{aF}$ used as input. With the inconsistent combination of $d_{vi} = 2.2$ Å (i.e., defect associate) and $\Delta G^{\ominus}_{aF}$ (i.e., infinite separation), one finds E^{aF}_{crit} in the range of (123 to 85) MV cm^{-1} for the temperature range (2000 to 2875) K, roughly an order of magnitude higher than the observed values. A consistent combination of $\Delta G^{\ominus}_{aF}$ and d_{vi} with both quantities referring to the same configuration, i.e., to the second or third configuration in eq 19, is characterized by a much lower $\Delta G^{\ominus}_{aF}$,[65,92] thus leading to better agreement. In other words, we find no evidence invalidating eq 3; rather, we draw attention to the problems involved in using it, and we emphasize the need for an improved, quantitative treatment.

A quantitative model encapsulating the three reaction steps of eq 19 would involve a considerable number of parameters since each step would require a few characteristic parameters. It would possibly yield, if at all, an unwieldy expression for $\Delta H^{\ominus}_{aF,eff}$. Hence, instead of considering such an exact model, we formulate a simpler, effective model in which we assume that anti-Frenkel pair generation can be described approximately by the Gibbs energy landscape shown in Figure 9a. The landscape is

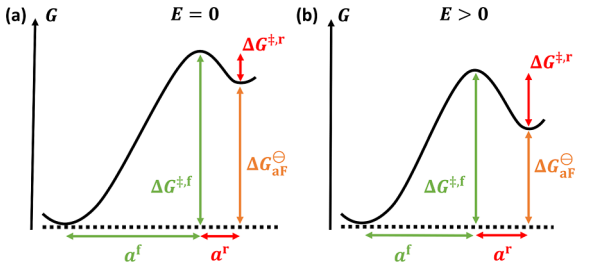

Figure 9. Simple model of field-driven anti-Frenkel disorder, showing Gibbs energy landscapes for the formation and recombination of oxygen vacancies and oxygen interstitials through the anti-Frenkel disorder reaction (a) without applied field and (b) with an applied field E. For the formation, the ion needs to traverse the distance a^f to overcome the barrier $\Delta G^{\ddagger,f}$, and for the recombination, the distance a^r and the barrier $\Delta G^{\ddagger,r}$. The difference between the initial and final states equals the free enthalpy of anti-Frenkel defect formation, $\Delta G^{\ominus}_{aF} = \Delta G^{\ddagger,f} - \Delta G^{\ddagger,r}$.

characterized by a comparatively high barrier $\Delta G^{\ddagger,f}$ for the formation of the defect pair and a small but nonzero barrier $\Delta G^{\ddagger,r}$ for the recombination (as indicated in the figure, $\Delta G^{\ddagger,f} = \Delta G^{\ominus}_{aF} + \Delta G^{\ddagger,r}$).

The reaction rate for anti-Frenkel formation can be written from standard chemical kinetics as

$$\nu = k^f c_{is} c_O - k^r c_i c_v \tag{20}$$

with rate constants k^f and k^r for charge-carrier formation and recombination, respectively. Expressing the rate constants $k^{f/r}$ in

https://doi.org/10.1021/jacs.3c12843
J. Am. Chem. Soc. 2024, 146, 4783−4794

terms of the respective attempt frequencies and Gibbs energies, that is, as $\nu_0^{f/r}\exp[-\Delta G^{\ddagger,f/r}/(k_BT)]$, one recovers at equilibrium ($v = 0$)

$$\frac{c_i c_v}{c_{is} c_O} = \frac{\nu_0^f \exp\left(\frac{-\Delta G^{\ddagger,f}}{k_BT}\right)}{\nu_0^r \exp\left(\frac{-\Delta G^{\ddagger,r}}{k_BT}\right)} = \exp\left(-\frac{\Delta G_{aF}^{\ominus}}{k_BT}\right) = K_{aF} \tag{21}$$

i.e., the equilibrium constant of anti-Frenkel disorder. If an electric field is applied to the system, this will result in a decrease of $\Delta G^{\ddagger,f}$ and an increase of $\Delta G^{\ddagger,r}$, as shown in Figure 9b. Assuming that, as in the traditional treatment,[22−24] $\Delta G^{\ddagger,f/r}$ is modified by the applied electric field according to

$$\Delta G^{\ddagger,f/r}(E) = \Delta G^{\ddagger,f/r} \mp |z_j| eEa^{f/r} \tag{22}$$

and assuming further that $a^f \approx a^r = d_{vi}/2$ and $\nu_0{}^f = \nu_0{}^r$, one finds that the field-dependent equilibrium constant of anti-Frenkel disorder is

$$K_{aF}(E) = \exp\left(-\frac{\Delta G_{aF}^{\ominus} - |z_j| eEd_{vi}}{k_BT}\right) \tag{23}$$

By applying eq 18, one then obtains

$$\Delta H_{aF,eff}^{\ominus} = \Delta H_{aF}^{\ominus} - |z_j| eEd_{vi} \tag{24}$$

A comparison between this prediction and the MD-derived data for $\Delta H_{aF,eff}^{\ominus}$ in Figure 8 (dashed line) reveals good agreement up to 7 MV cm^{-1} but an underestimation of the decrease in $\Delta H_{aF,eff}^{\ominus}$ at higher field strengths.

A superior approach to eq 22 is to assume a mathematical form for the Gibbs energy landscape and to superimpose the field linearly onto it. This is analogous to the treatment of field-driven ion mobility by Genreith-Schriever and De Souza[68] (see Section 1.2). Here, we assume that each Gibbs energy barrier sketched in Figure 9 has a cosinusoidal form, such that a linearly superimposed electric field leads to the equivalent forms of eq 6 for $\Delta G^{\ddagger,f/r}(E)$. Since this does not produce a simple expression for $\Delta H_{aF,eff}^{\ominus}$, we expand the (f/r) forms of eq 6 to obtain

$$\Delta G^{\ddagger,f/r}(E) = \Delta G^{\ddagger,f/r}\left[1 \mp \frac{\gamma^{f/r}\pi}{2} + \frac{(\gamma^{f/r})^2}{2} + \frac{(\gamma^{f/r})^4}{24} + \frac{(\gamma^{f/r})^6}{80} + \ldots\right] \tag{25}$$

with

$$\gamma^{f/r} = \frac{2|z_j| eEa^{f/r}}{\pi \Delta G^{\ddagger,f/r}} \tag{26}$$

Truncating eq 25 after the quadratic terms, combining the result with eqs 21 and 26, and assuming $a^f \approx a^r = d_{vi}/2$ gives

$$K_{aF}(E) = \exp\left[-\frac{\Delta G_{aF}^{\ominus} - |z_j| eEd_{vi} + 2\left(\frac{|z_j| eEd_{vi}}{2\pi}\right)^2\left(\frac{1}{\Delta G^{\ddagger,f}} - \frac{1}{\Delta G^{\ddagger,r}}\right)}{k_BT}\right] \tag{27}$$

Since $\Delta G^{\ddagger,r} \ll \Delta G^{\ddagger,f}$ (see Figure 9) and assuming, for simplicity, $\Delta G^{\ddagger,r} \approx \Delta H^{\ddagger,r}$, we finally obtain by applying eq 18

$$\Delta H_{aF,eff}^{\ominus} = \Delta H_{aF}^{\ominus} - |z_j| eEd_{vi} - 2\left(\frac{|z_j| eEd_{vi}}{2\pi}\right)^2 \frac{1}{\Delta H^{\ddagger,r}} \tag{28}$$

With this expression, $\Delta H_{aF,eff}^{\ominus}$ can be described satisfactorily over the whole field-strength range with $\Delta H^{\ddagger,r} = 9$ meV (solid line in Figure 8), although given the large error bars, descriptions with $\Delta H^{\ddagger,r}$ from 5 up to 18 meV are possible. The difference between the two curves in Figure 8 illustrates the importance of taking the form of the free energy landscape into account, as this leads to an additional (quadratic) field term in eq 28. A second important point illustrated by eq 28 is the nonzero, field-dependent barrier for recombination, $\Delta H^{\ddagger,r}$. The value of $\Delta H^{\ddagger,r}$ obtained is essentially a doubly effective quantity; it is effective because of the simplified model and because of the assumptions made in the derivation. Nevertheless, from its order of magnitude, it is in agreement with computational studies[65,95] that report fast recombination of neighboring oxygen vacancies and interstitials in AO_2 fluorites, extracting from the recombination kinetics effective activation energies of some tens of meV.

3.3.2. Prediction of Field-Dependent Oxide-Ion Mobilities. Combining eqs 4−6, 14, 28, and using $\Delta H^{\ddagger,r} = 18$ meV, we predict $u_O(E,T)$ for LZO for the whole temperature and field strength range. As seen in Figure 10 for $T > 2125$ K, an excellent description of u_O is observed over the entire field strength range. At lower temperatures, it is unclear whether the mobilities are satisfactorily described due to poor data quality. The excellent description at higher temperatures, however, suggests that the predictions at lower temperatures are trustworthy.

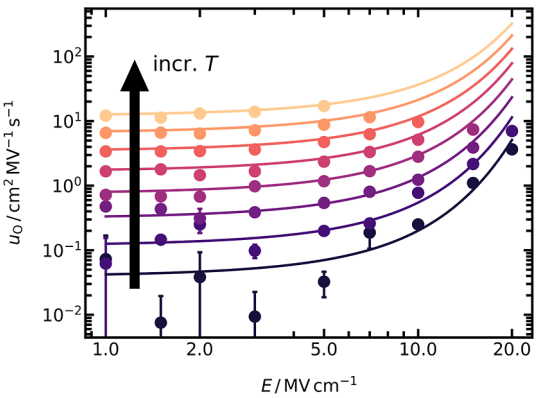

Figure 10. Field-dependent oxide-ion mobilities u_O obtained from MD simulations of LZO in the range of $2000 \le T/K \le 2875$. Every data point is the average of two independent runs, with their standard deviation included as error bars. Solid lines are predictions calculated with a combination of eqs 4−6, 14, 28. For the predictions, $\Delta H_{aF}^{\ominus} = (5.32 \pm 0.01)$ eV and $\Delta S_{aF}^{\ominus} = (11.48 \pm 0.22)\, k_B$ from Figure 3 are used; and $\Delta H^{\ddagger,r} = 18$ meV.

We can predict with some confidence, therefore, the behavior at much lower temperatures, i.e., at those more appropriate to experiment or device. At $T = 500$ K, for example, we predict that a field of 5 MV cm^{-1} is sufficient to increase the concentration of anti-Frenkel defects by 1 order of magnitude. Such a field is achieved by applying a potential difference of 1 V to a film of 2 nm thickness. It does not involve, therefore, potential differences of several volts, which are sufficient for phase decomposition, or film thickness below a unit cell. Since such a field also increases the vacancy mobility in LZO by a factor of 1.5, one can attain an increase in conductivity by a factor of 15. Consequently, utilizing this effect in actual devices is not limited by physical constraints;

https://doi.org/10.1021/jacs.3c12843
J. Am. Chem. Soc. 2024, 146, 4783−4794

instead, we contend that fabricating high-quality, stable devices will be the major problem. Predicting the behavior of other pyrochlore systems,or indeed, other material systems, is difficult since it is unclear how the effective quantity $\Delta H^{\ddagger,r}$ varies from system to system. Simulation studies of a range of pyrochlore compositions are thus required to make the next step of progress toward hitting the two birds of defect behavior with the one stone of an electric field.

4. CONCLUSIONS

In this study, we demonstrated how to successfully hit the two birds of defect mobility and defect concentration with the stone of a high electric field. To this end, field- and temperature-dependent ion mobilities u_O for oxygen-deficient, oxygen-rich, and stoichiometric $La_2Zr_2O_7$ (LZO) were determined from MD simulations employing many-body potentials. Three important points are highlighted:

(1) Based on an effective free energy landscape of anti-Frenkel formation, we derived an expression to predict quantitatively $c_{def}(E,T)$. The importance of field-dependent energy barriers for defect formation and recombination is emphasized.

(2) According to our treatment, ionic charge-carrier concentrations in a pyrochlore oxide can be increased by orders of magnitude without the need for aliovalent doping or cation disorder and within the thermodynamic stability window of the material through the application of a high electric field.

(3) We present three methods based on three different system properties to obtain oxygen-vacancy and oxygen-interstitial concentrations, and thus $\Delta H^{\ominus}_{aF}$ and $\Delta S^{\ominus}_{aF}$, directly from MD simulations: combination of defect mobilities, WS analysis, and excess heat capacity analysis. Satisfyingly, all three methods agree very well with each other, yielding $\Delta H^{\ominus}_{aF} \approx (5.2 \pm 0.1)$ eV and $\Delta S^{\ominus}_{aF} \approx (12 \pm 1)\ k_B$.

AUTHOR INFORMATION

Corresponding Authors

Dennis Kemp − *Institute of Physical Chemistry, RWTH Aachen University, 52056 Aachen, Germany;* orcid.org/0000-0003-1237-159X; Phone: +49 241 80 98617; Email: kemp@pc.rwth-aachen.de

Roger A. De Souza − *Institute of Physical Chemistry, RWTH Aachen University, 52056 Aachen, Germany;* orcid.org/0000-0001-7721-4128; Email: desouza@pc.rwth-aachen.de

Complete contact information is available at: https://pubs.acs.org/10.1021/jacs.3c12843

Notes

The authors declare no competing financial interest.

The English idiom is “To kill two birds with one stone”.

ACKNOWLEDGMENTS

Funding by the Deutsche Forschungsgemeinschaft (DFG, German Research Foundation)—167917811—within the framework of the collaborative research center Nanoswitches (SFB 917) is acknowledged. This project received funding from the European Union’s Horizon 2020 research and innovation program under grant agreement no. 101017709 (EPISTORE). Simulations were performed with computing resources granted by RWTH Aachen University under Project no. p0020103.

REFERENCES

(1) Etsell, T. H.; Flengas, S. N. Electrical Properties of Solid Oxide Electrolytes. *Chem. Rev.* **1970**, *70*, 339−376.

(2) Steele, B. C. H. Oxygen Ion Conductors and Their Technological Applications. *Mater. Sci. Eng., B* **1992**, *13*, 79−87.

(3) Skinner, S. J.; Kilner, J. A. Oxygen Ion Conductors. *Mater. Today* **2003**, *6*, 30−37.

(4) Goodenough, J. B. Oxide-Ion Electrolytes. *Annu. Rev. Mater. Res.* **2003**, *33*, 91−128.

(5) Kharton, V.; Marques, F.; Atkinson, A. Transport Properties of Solid Oxide Electrolyte Ceramics: A Brief Review. *Solid State Ionics* **2004**, *174*, 135−149.

(6) Kendrick, E.; Islam, M. S.; Slater, P. R. Developing Apatites for Solid Oxide Fuel Cells: Insight into Structural, Transport and Doping Properties. *J. Mater. Chem.* **2007**, *17*, 3104.

(7) Malavasi, L.; Fisher, C. A. J.; Islam, M. S. Oxide-Ion and Proton Conducting Electrolyte Materials for Clean Energy Applications: Structural and Mechanistic Features. *Chem. Soc. Rev.* **2010**, *39*, 4370.

(8) Boivin, J. C.; Mairesse, G. Recent Material Developments in Fast Oxide Ion Conductors. *Chem. Mater.* **1998**, *10*, 2870−2888.

(9) Figueiredo, F. M. L.; Marques, F. M. B. Electrolytes for Solid Oxide Fuel Cells: Electrolytes for Solid Oxide Fuel Cells. *WIRES Energy Environ.* **2013**, *2*, 52−72.

(10) De Souza, R. A. Limits to the Rate of Oxygen Transport in Mixed-Conducting Oxides. *J. Mater. Chem. A* **2017**, *5*, 20334−20350.

(11) Navickas, E.; Huber, T. M.; Chen, Y.; Hetaba, W.; Holzlechner, G.; Rupp, G.; Stöger-Pollach, M.; Friedbacher, G.; Hutter, H.; Yildiz, B.; Fleig, J. Fast Oxygen Exchange and Diffusion Kinetics of Grain Boundaries in Sr-doped $LaMnO_3$ Thin Films. *Phys. Chem. Chem. Phys.* **2015**, *17*, 7659−7669.

(12) De Souza, R. A.; Pietrowski, M. J.; Anselmi-Tamburini, U.; Kim, S.; Munir, Z. A.; Martin, M. Oxygen Diffusion in Nanocrystalline Yttria-Stabilized Zirconia: The Effect of Grain Boundaries. *Phys. Chem. Chem. Phys.* **2008**, *10*, 2067.

(13) Knöner, G.; Reimann, K.; Röwer, R.; Södervall, U.; Schaefer, H.-E. Enhanced Oxygen Diffusivity in Interfaces of Nanocrystalline ZrO_2·Y_2O_3. *Proc. Natl. Acad. Sci. U.S.A.* **2003**, *100*, 3870−3873.

(14) Saranya, A. M.; Pla, D.; Morata, A.; Cavallaro, A.; Canales-Vázquez, J.; Kilner, J. A.; Burriel, M.; Tarancón, A. Engineering Mixed Ionic Electronic Conduction in $La_{0.8}Sr_{0.2}MnO_{3+\delta}$ Nanostructures through Fast Grain Boundary Oxygen Diffusivity. *Adv. Energy Mater.* **2015**, *5*, 1500377.

(15) Garcia-Barriocanal, J.; Rivera-Calzada, A.; Varela, M.; Sefrioui, Z.; Iborra, E.; Leon, C.; Pennycook, S. J.; Santamaria, J. Colossal Ionic Conductivity at Interfaces of Epitaxial ZrO_2:Y_2O_3/$SrTiO_3$ Heterostructures. *Science* **2008**, *321*, 676−680.

(16) Kushima, A.; Yildiz, B. Oxygen Ion Diffusivity in Strained Yttria Stabilized Zirconia: Where Is the Fastest Strain? *J. Mater. Chem.* **2010**, *20*, 4809.

(17) De Souza, R. A.; Ramadan, A.; Hörner, S. Modifying the Barriers for Oxygen-Vacancy Migration in Fluorite-Structured CeO_2 Electrolytes through Strain: A Computer Simulation Study. *Energy Environ. Sci.* **2012**, *5*, 5445−5453.

(18) Harrington, G. F.; Sun, L.; Yildiz, B.; Sasaki, K.; Perry, N. H.; Tuller, H. L. The Interplay and Impact of Strain and Defect Association on the Conductivity of Rare-Earth Substituted Ceria. *Acta Mater.* **2019**, *166*, 447−458.

(19) Harrington, G. F.; Kim, S.; Sasaki, K.; Tuller, H. L.; Grieshammer, S. Strain-Modified Ionic Conductivity in Rare-Earth Substituted Ceria: Effects of Migration Direction, Barriers, and Defect-Interactions. *J. Mater. Chem. A* **2021**, *9*, 8630−8643.

(20) De Souza, R. A.; Ramadan, A. H. H. Ionic Conduction in the $SrTiO_3$—YSZ—$SrTiO_3$ Heterostructure. *Phys. Chem. Chem. Phys.* **2013**, *15*, 4505.

(21) Fluri, A.; Pergolesi, D.; Roddatis, V.; Wokaun, A.; Lippert, T. In Situ Stress Observation in Oxide Films and How Tensile Stress Influences Oxygen Ion Conduction. *Nat. Commun.* **2016**, *7*, 10692.

(22) Verwey, E. Electrolytic Conduction of a Solid Insulator at High Fields The Formation of the Anodic Oxide Film on Aluminium. *Physica* **1935**, *2*, 1059−1063.
(23) Mott, N. F.; Gurney, R. W. *Electronic Processes in Ionic Crystals*; Clarendon Press: Oxford, 1940.
(24) Frenkel, J. *Kinetic Theory of Liquids*; Oxford University Press: Oxford, 1946.
(25) Roling, B.; Murugavel, S.; Heuer, A.; Lühning, L.; Friedrich, R.; Röthel, S. Field-Dependent Ion Transport in Disordered Solid Electrolytes. *Phys. Chem. Chem. Phys.* **2008**, *10*, 4211−4226.
(26) Dignam, M. Ion Transport in Solids under Conditions Which Include Large Electric Fields. *J. Phys. Chem. Solids* **1968**, *29*, 249−260.
(27) Murugavel, S.; Roling, B. Application of Nonlinear Conductivity Spectroscopy to Ion Transport in Solid Electrolytes. *J. Non-Cryst. Solids* **2005**, *351*, 2819−2824.
(28) Kunow, M.; Heuer, A. Nonlinear Ionic Conductivity of Lithium Silicate Glass Studied via Molecular Dynamics Simulations. *J. Chem. Phys.* **2006**, *124*, 214703.
(29) Menzel, S.; Waters, M.; Marchewka, A.; Böttger, U.; Dittmann, R.; Waser, R. Origin of the Ultra-nonlinear Switching Kinetics in Oxide-Based Resistive Switches. *Adv. Funct. Mater.* **2011**, *21*, 4487−4492.
(30) Xu, Z.; Rosso, K. M.; Bruemmer, S. Metal Oxidation Kinetics and the Transition from Thin to Thick Films. *Phys. Chem. Chem. Phys.* **2012**, *14*, 14534.
(31) Menzel, S.; von Witzleben, M.; Havel, V.; Böttger, U. The Ultimate Switching Speed Limit of Redox-Based Resistive Switching Devices. *Faraday Discuss.* **2019**, *213*, 197−213.
(32) Strukov, D. B.; Williams, R. S. Exponential Ionic Drift: Fast Switching and Low Volatility of Thin-Film Memristors. *Appl. Phys. A: Mater. Sci. Process.* **2009**, *94*, 515−519.
(33) Kröger, F.; Vink, H. *Solid State Physics*; Elsevier, 1956; Vol. *3*, pp 307−435.
(34) Norby, T. A Kr Öger-Vink Compatible Notation for Defects in Inherently Defective Sublattices. *J. Korean Ceram. Soc.* **2010**, *47*, 19−25.
(35) De Souza, R. A.; Harrington, G. Revisiting Point Defects in Ionic Solids and Semiconductors. *Nat. Mater.* **2023**, *22*, 794−797.
(36) Akhtar, M. J.; Akhtar, Z.-U.-N.; Jackson, R. A.; Catlow, C. R. A. Computer Simulation Studies of Strontium Titanate. *J. Am. Ceram. Soc.* **1995**, *78*, 421−428.
(37) Thomas, B. S.; Marks, N. A.; Begg, B. D. Defects and Threshold Displacement Energies in $SrTiO_3$ Perovskite Using Atomistic Computer Simulations. *Nucl. Instrum. Methods Phys. Res., Sect. B* **2007**, *254*, 211−218.
(38) De Souza, R. A.; Islam, M. S.; Ivers-Tiffée, E. Formation and Migration of Cation Defects in the Perovskite Oxide $LaMnO_3$. *J. Mater. Chem.* **1999**, *9*, 1621−1627.
(39) Ambaum, S.; Spinger, S.; De Souza, R. A. in preparation.
(40) Wilde, P. J.; Catlow, C. R. A. Molecular Dynamics Study of the Effect of Doping and Disorder on Diffusion in Gadolinium Zirconate. *Solid State Ionics* **1998**, *112*, 185−195.
(41) Li, Y.; Kowalski, P. M. Energetics of Defects Formation and Oxygen Migration in Pyrochlore Compounds from First Principles Calculations. *J. Nucl. Mater.* **2018**, *505*, 255−261.
(42) Wang, P.; Zhao, J.; Fan, Y.; Zhang, W.; Cui, Y.; Zhang, L.; Liu, B.; Nian, H.; Li, Y. Theoretical Investigation of Intrinsic Point Defects and the Oxygen Migration Behavior in Rare Earth Hafnates. *Ceram. Int.* **2021**, *47*, 15023−15029.
(43) Pirzada, M.; Grimes, R. W.; Minervini, L.; Maguire, J. F.; Sickafus, K. E. Oxygen Migration in $A_2B_2O_7$ Pyrochlores. *Solid State Ionics* **2001**, *140*, 201−208.
(44) Perriot, R.; Uberuaga, B. P. Structural vs. Intrinsic Carriers: Contrasting Effects of Cation Chemistry and Disorder on Ionic Conductivity in Pyrochlores. *J. Mater. Chem. A* **2015**, *3*, 11554−11565.
(45) Moon, P. K.; Tuller, H. L. Ionic Conduction in the $Gd_2Ti_2O_7$-$Gd_2Zr_2O_7$ System. *Solid State Ionics* **1988**, *28*−*30*, 470−474.
(46) Tuller, H. L. Oxygen Ion Conduction and Structural Disorder in Conductive Oxides. *J. Phys. Chem. Solids* **1994**, *55*, 1393−1404.
(47) Kramer, S.; Spears, M.; Tuller, H. Conduction in Titanate Pyrochlores: Role of Dopants. *Solid State Ionics* **1994**, *72*, 59−66.
(48) Yu, T.-H.; Tuller, H. L. Ionic Conduction and Disorder in the $Gd_2Sn_2O_7$ Pyrochlore System. *Solid State Ionics* **1996**, *86*−*88*, 177−182.
(49) Frechero, M.; Durá, O.; Díaz-Guillén, M.; Moreno, K.; Díaz-Guillén, J.; García-Barriocanal, J.; Rivera-Calzada, A.; Fuentes, A.; León, C. Oxygen Ion Dynamics in Pyrochlore-Type Ionic Conductors: Effects of Structure and Ion−Ion Cooperativity. *J. Non-Cryst. Solids* **2015**, *407*, 349−354.
(50) Cooper, M. W. D.; Rushton, M. J. D.; Grimes, R. W. A Many-Body Potential Approach to Modelling the Thermomechanical Properties of Actinide Oxides. *J. Phys.: Condens. Matter* **2014**, *26*, 105401.
(51) Liu, X.-Y.; Cooper, M. W. D.; McClellan, K. J.; Lashley, J. C.; Byler, D. D.; Bell, B. D. C.; Grimes, R. W.; Stanek, C. R.; Andersson, D. A. Molecular Dynamics Simulation of Thermal Transport in UO_2 Containing Uranium, Oxygen, and Fission-product Defects. *Phys. Rev. Appl.* **2016**, *6*, 044015.
(52) Minervini, L.; Grimes, R. W.; Sickafus, K. E. Disorder in Pyrochlore Oxides. *J. Am. Ceram. Soc.* **2000**, *83*, 1873−1878.
(53) Michel, D.; Perez Y Jorba, M.; Collongues, R. Etude de la transformation ordre-desordre de la structure fluorite a la structure pyrochlore pour des phases (1-x) ZrO_2-x Ln_2O_3. *Mater. Res. Bull.* **1974**, *9*, 1457−1468.
(54) Ushakov, S. V.; Navrotsky, A.; Weber, R. J. K.; Neuefeind, J. C. Structure and Thermal Expansion of YSZ and $La_2Zr_2O_7$ Above 1500°C from Neutron Diffraction on Levitated Samples. *J. Am. Ceram. Soc.* **2015**, *98*, 3381−3388.
(55) Jiang, C.; Stanek, C. R.; Sickafus, K. E.; Uberuaga, B. P. First-Principles Prediction of Disordering Tendencies in Pyrochlore Oxides. *Phys. Rev. B: Condens. Matter Mater. Phys.* **2009**, *79*, 104203.
(56) Li, Y.; Kowalski, P. M.; Beridze, G.; Birnie, A. R.; Finkeldei, S.; Bosbach, D. Defect Formation Energies in $A_2B_2O_7$ Pyrochlores. *Scr. Mater.* **2015**, *107*, 18−21.
(57) Strand, J. W.; Cottom, J.; Larcher, L.; Shluger, A. L. Effect of Electric Field on Defect Generation and Migration in HfO_2. *Phys. Rev. B* **2020**, *102*, 014106.
(58) Salles, N.; Martin-Samos, L.; de Gironcoli, S.; Giacomazzi, L.; Valant, M.; Hemeryck, A.; Blaise, P.; Sklenard, B.; Richard, N. Defect Creation and Diffusion under Electric Fields from First-Principles: The Prototypical Case of Silicon Dioxide. *International Conference on Simulation of Semiconductor Processes and Devices SISPAD*, 2019; pp 1−4.
(59) Abdelouahed, S.; McKenna, K. P. Relevance of Non-Equilibrium Defect Generation Processes to Resistive Switching in TiO_2. *J. Appl. Phys.* **2015**, *118*, 134103.
(60) Youssef, M.; Van Vliet, K. J.; Yildiz, B. Polarizing Oxygen Vacancies in Insulating Metal Oxides under a High Electric Field. *Phys. Rev. Lett.* **2017**, *119*, 126002.
(61) Chi, Y.-T.; Van Vliet, K. J.; Youssef, M.; Yildiz, B. Complex Oxides under Simulated Electric Field: Determinants of Defect Polarization in ABO_3 Perovskites. *Advanced Science* **2022**, *9*, 2104476.
(62) Xu, W.; Maksymenko, A.; Hasan, S.; Meléndez, J. J.; Olevsky, E. Effect of External Electric Field on Diffusivity and Flash Sintering of 8YSZ: A Molecular Dynamics Study. *Acta Mater.* **2021**, *206*, 116596.
(63) Guillon, O.; De Souza, R. A.; Mishra, T. P.; Rheinheimer, W. Electric-Field-Assisted Processing of Ceramics: Nonthermal Effects and Related Mechanisms. *MRS Bull.* **2021**, *46*, 52−58.
(64) Hammond, K. D. Parallel Point Defect Identification in Molecular Dynamics Simulations without Post-Processing: A Compute and Dump Style for LAMMPS. *Comput. Phys. Commun.* **2020**, *247*, 106862.
(65) Schie, M.; Menzel, S.; Robertson, J.; Waser, R.; De Souza, R. A. Field-Enhanced Route to Generating Anti-Frenkel Pairs in HfO_2. *Phys. Rev. Mater.* **2018**, *2*, 035002.
(66) Evans, D. M.; Holstad, T. S.; Mosberg, A. B.; Småbråten, D. R.; Vullum, P. E.; Dadlani, A. L.; Shapovalov, K.; Yan, Z.; Bourret, E.; Gao, D.; Akola, J.; Torgersen, J.; van Helvoort, A. T. J.; Selbach, S. M.; Meier, D. Conductivity Control via Minimally Invasive Anti-Frenkel Defects in a Functional Oxide. *Nat. Mater.* **2020**, *19*, 1195−1200.

https://doi.org/10.1021/jacs.3c12843
J. Am. Chem. Soc. 2024, 146, 4783−4794

(67) Evans, D. M.; Småbråten, D. R.; Holstad, T. S.; Vullum, P. E.; Mosberg, A. B.; Yan, Z.; Bourret, E.; van Helvoort, A. T. J.; Selbach, S. M.; Meier, D. Observation of Electric-Field-Induced Structural Dislocations in a Ferroelectric Oxide. *Nano Lett.* **2021**, *21*, 3386−3392.
(68) Genreith-Schriever, A. R.; De Souza, R. A. Field-Enhanced Ion Transport in Solids: Reexamination with Molecular Dynamics Simulations. *Phys. Rev. B* **2016**, *94*, 224304.
(69) Calvaresi, M.; Martinez, R. V.; Losilla, N. S.; Martinez, J.; Garcia, R.; Zerbetto, F. Splitting CO_2 with Electric Fields: A Computational Investigation. *J. Phys. Chem. Lett.* **2010**, *1*, 3256−3260.
(70) Hirao, H.; Chen, H.; Carvajal, M. A.; Wang, Y.; Shaik, S. Effect of External Electric Fields on the C-H Bond Activation Reactivity of Nonheme Iron-Oxo Reagents. *J. Am. Chem. Soc.* **2008**, *130*, 3319−3327.
(71) Thompson, A. P.; Aktulga, H. M.; Berger, R.; Bolintineanu, D. S.; Brown, W. M.; Crozier, P. S.; in't Veld, P. J.; Kohlmeyer, A.; Moore, S. G.; Nguyen, T. D.; Shan, R.; Stevens, M. J.; Tranchida, J.; Trott, C.; Plimpton, S. J. LAMMPS - a Flexible Simulation Tool for Particle-Based Materials Modeling at the Atomic, Meso, and Continuum Scales. *Comput. Phys. Commun.* **2022**, *271*, 108171.
(72) Hoover, W. G. Canonical Dynamics: Equilibrium Phase-Space Distributions. *Phys. Rev. A: At., Mol., Opt. Phys.* **1985**, *31*, 1695−1697.
(73) Nosé, S. A Unified Formulation of the Constant Temperature Molecular Dynamics Methods. *J. Chem. Phys.* **1984**, *81*, 511−519.
(74) Hockney, R. W. *Computer Simulation Using Particles*; CRC Press: Boca Raton, 1988.
(75) Kemp, D.; Tarancón, A.; De Souza, R. A. Recipes for Superior Ionic Conductivities in Thin-Film Ceria-Based Electrolytes. *Phys. Chem. Chem. Phys.* **2022**, *42*, 12926−12936.
(76) Daw, M. S.; Baskes, M. I. Embedded-Atom Method: Derivation and Application to Impurities, Surfaces, and Other Defects in Metals. *Phys. Rev. B: Condens. Matter Mater. Phys.* **1984**, *29*, 6443−6453.
(77) Rushton, M. J. D.; Chroneos, A. Impact of Uniaxial Strain and Doping on Oxygen Diffusion in CeO_2. *Sci. Rep.* **2014**, *4*, 6068.
(78) Kutty, K.; Rajagopalan, S.; Mathews, C.; Varadaraju, U. Thermal Expansion Behaviour of Some Rare Earth Oxide Pyrochlores. *Mater. Res. Bull.* **1994**, *29*, 759−766.
(79) Labrincha, J. A.; Frade, J. R.; Marques, F. M. B. La2Zr2O7 Formed at Ceramic Electrode/YSZ Contacts. *J. Mater. Sci.* **1993**, *28*, 3809−3815.
(80) Hagiwara, T.; Yamamura, H.; Nishino, H. Relationship Between Oxide-Ion Conductivity and Ordering of Oxygen Vacancy in the $Ln_2Zr_2O_7$ (Ln = La, Nd, Eu) System Using High Temperature XRD. *J. Fuel Cell Sci. Technol.* **2011**, *8*, 051020.
(81) Chartier, A.; Meis, C.; Weber, W. J.; Corrales, L. R. Theoretical Study of Disorder in Ti-substituted $La_2Zr_2O_7$. *Phys. Rev. B: Condens. Matter Mater. Phys.* **2002**, *65*, 134116.
(82) Shimamura, K.; Arima, T.; Idemitsu, K.; Inagaki, Y. Thermophysical Properties of Rare-Earth-Stabilized Zirconia and Zirconate Pyrochlores as Surrogates for Actinide-Doped Zirconia. *Int. J. Thermophys.* **2007**, *28*, 1074−1084.
(83) Kawano, T.; Muta, H.; Uno, M.; Ohishi, Y.; Kurosaki, K.; Yamanaka, S. Characterization and Thermomechanical Properties of $Ln_2Zr_2O_7$ (Ln = La, Pr, Nd, Eu, Gd, Dy) and $Nd_2Ce_2O_7$. *MRS Proc.* **2013**, *1514*, 139−144.
(84) Antonova, E.; Tropin, E.; Khodimchuk, A. Alkaline Earth−Doped $La_2Zr_2O_7$ Oxides with a Pyrochlore Structure: Phase Equilibria and Electrical Properties. *Ionics* **2022**, *28*, 5181−5188.
(85) Huo, D.; Baldinozzi, G.; Siméone, D.; Khodja, H.; Surblé, S. Grain Size-Dependent Electrical Properties of $La_{1.95}Sr_{0.05}Zr_2O_{7-\delta}$ as Potential Proton Ceramic Fuel Cell Electrolyte. *Solid State Ionics* **2016**, *298*, 35−43.
(86) Stukowski, A. Visualization and Analysis of Atomistic Simulation Data with OVITO−the Open Visualization Tool. *Modelling Simul. Mater. Sci. Eng.* **2010**, *18*, 015012.
(87) Kobayashi, K. Heat Capacity and Lattice Defects of Silver Chloride. *Phys. Rev.* **1952**, *85*, 150−151.
(88) Kanzaki, H. Lattice Defects in Silver Bromide. *Phys. Rev.* **1951**, *81*, 884.
(89) Christy, R. W.; Lawson, A. W. High Temperature Specific Heat of AgBr. *J. Chem. Phys.* **1951**, *19*, 517.
(90) Yang, L.; Wang, P.; Zhang, C.; Liu, Y.; Cui, Y.; Zhang, L.; Liu, B. Composition-dependent Intrinsic Defect Structures in Pyroclore $RE_2B_2O_7$ (RE = La, Nd, Gd; B = Sn, Hf, Zr). *J. Am. Ceram. Soc.* **2020**, *103*, 645−655.
(91) Grieshammer, S.; Zacherle, T.; Martin, M. Entropies of Defect Formation in Ceria from First Principles. *Phys. Chem. Chem. Phys.* **2013**, *15*, 15935.
(92) Walsh, A.; Woodley, S. M.; Catlow, C. R. A.; Sokol, A. A. Potential Energy Landscapes for Anion Frenkel-pair Formation in Ceria and India. *Solid State Ionics* **2011**, *184*, 52−56.
(93) Kreller, C. R.; Valdez, J. A.; Holesinger, T. G.; Morgan, J.; Wang, Y.; Tang, M.; Garzon, F. H.; Mukundan, R.; Brosha, E. L.; Uberuaga, B. P. Massively Enhanced Ionic Transport in Irradiated Crystalline Pyrochlore. *J. Mater. Chem. A* **2019**, *7*, 3917−3923.
(94) Kemp, D.; De Souza, R. A. Nonlinear Ion Mobility at High Electric Field Strengths in the Perovskites $SrTiO_3$ and $CH_3NH_3PbI_3$. *Phys. Rev. Mater.* **2021**, *5*, 105401.
(95) Pannier, N.; Guglielmetti, A.; Van Brutzel, L.; Chartier, A. Molecular Dynamics Study of Frenkel Pair Recombinations in Fluorite Type Compounds. *Nucl. Instrum. Methods Phys. Res., Sect. B* **2009**, *267*, 3118−3121.

https://doi.org/10.1021/jacs.3c12843
J. Am. Chem. Soc. 2024, 146, 4783−4794